Available online at www.sciencedirect.com

ScienceDirect

Acta Materialia 86 (2015) 157–168

Acta MATERIALIA

www.elsevier.com/locate/actamat

Failure mechanisms in thin-walled nanocrystalline cylinders under uniaxial compression

Eral Bele,* Chandra Veer Singh and Glenn David Hibbard

Department of Materials Science and Engineering, University of Toronto, 184 College Street, Toronto, Ontario, Canada

Received 6 August 2014; revised 12 November 2014; accepted 25 November 2014
Available online 5 January 2015

Abstract—Lattice materials composed of hollow nanocrystalline struts have recently made it possible to access new regions of material property space, by exploiting structural efficiencies along multiple length scales (nanometre to centimetre range). An important design issue for these materials is to understand how the failure mechanisms that act at these scales affect the macroscopic mechanical properties. In this study, we tested hollow nanocrystalline cylinders of two different grain sizes (20 nm and 100 nm) in uniaxial compression to investigate the effect of grain size on dominant failure mechanisms, and the influence of the latter on the compressive strength. The finite element method was used to model the interaction of the three observed failure mechanisms: shell buckling (SB), yielding (Y) and fracture (F). Depending on the grain size and geometry, the failure sequence can be SB–Y–F, Y–SB–F, SB–Y or Y–SB, the order of which has important implications in defining the limits of mechanical performance. One such implication is that when shell buckling occurs in the inelastic regime of the material, the macroscopic strength increase due to grain size refinement can be greater than the inherent yield strength increase of the material. Second, material fracture and shell buckling may not be competing failure mechanisms, which means that the effectiveness of grain size reduction in increasing the structural efficiency of cylindrical strut members can span the entire Hall–Petch range of the material.

Keywords: Nanocrystalline material; Buckling; Fracture; Cellular solids; Damage initiation

1. Introduction

The failure of engineering materials occurs through processes that span a range of length scales. A central issue in materials design is the understanding of mechanisms by which processes that occur at one length scale influence those that act at others. Phenomena that bridge dimensional ranges are especially important in the development of internally architectured materials, which have structural features that are deliberately controlled to span orders of magnitude [1,2].

One example of such materials is the class of microtruss assemblies, i.e. networks of beams, tubes or struts with characteristic dimensions in the nanometre to centimetre range [3–10]. Design efforts in this class of materials often involve three length scales. On the macroscopic (e.g. cm) scale, the architecture of the network is designed to be stretch-dominated so that externally applied loads are resolved axially along the interconnected network of internal struts; this strategy results in increasing the weight-specific strength and stiffness relative to cellular materials with bending-dominated deformation (see Refs. [1,2,11,12] for examples).

On an intermediate (e.g. micrometre to centimetre) scale, a particularly effective design approach is to use strut members with functionally efficient cross-sections (e.g. hollow tubes). Design of cross-sectional efficiency at this intermediate scale is very effective in increasing the weight-specific properties of the structural members, because the axial buckling stress is proportional to the strut's radius of gyration (defined as $\sqrt{I/A}$, where I and A are the cross-sectional second moment of area and area, respectively), which means that a given mass of material would provide a substantially higher buckling resistance when positioned away from the neutral bending axis of the strut [13–17].

A third level of design is directed at the scale of the grain size of the constituent material (e.g. nanometre to micrometre scale). One example is the deposition of high-strength, grain-refined sleeves on architecturally optimized precursor geometries, effectively creating an interconnected network of nanocrystalline tubes [5–10]. Using this concept, layers of Ni-based alloys with grain sizes in the 10-20 nm range have been deposited both on conventional foams [5,18] and microtruss architectures [6,19], creating metal/metal and metal/polymer hybrids. This reinforcement is particularly useful because of the high yield strength achievable from grain size reduction to the nanometre scale, and the positioning of the reinforcement away from the neutral bending axis of the struts. Removal of the precursor after electrodeposition makes possible the fabrication of ultralight structures; recently, for example, microlattices with

* Corresponding author at: Cambridge University Engineering Department, Trumpington Street, Cambridge, UK. Tel.: +44 7521530300; e-mail addresses: eral.bele@utoronto.ca; eral.bele@eng.cam.ac.uk

http://dx.doi.org/10.1016/j.actamat.2014.11.041
1359-6462/

hollow tube morphologies were fabricated at densities as low as 10^{-4} g cm^{-3} [7–10].

The reduction of the material's grain size to the nanocrystalline regime introduces new failure mechanisms whose interaction and influence on mechanical properties are not well understood. Under uniaxial compression alone, examples of failure mechanisms include fracture at the strut connective regions [5–9], local [20] or global [6,19] strut buckling and catastrophic fracture in the cylindrical walls [10,20]. In studies conducted so far, the role of the material's grain size on the failure mechanisms and mechanical properties of the cellular assembly has not been investigated. This analysis is complex due to two issues: the non-monotonic relationship between the strength of the assembly and that of the constitutive material, and the interaction between material failure and structural collapse.

First, the structural strength of stretching-dominated lattices is by definition determined by the axial deformation characteristics of the constituent struts, thus it is expected to increase in some proportion to the material's inherent yield strength increase owing to grain size refinement. However, in cases when instabilities occur in the inelastic regime of the material, the critical strength and strain of the column are dependent on both the geometry of the column (the slenderness ratio) and stress–strain relationship in the inelastic regime; the latter determines the function of the material's tangent modulus with strain. Generally, the work hardening capacity of the material is determined by the intracrystalline dislocation interaction, so a reduction in grain size also means that a lower tangent modulus is achieved.

Second, since the strength increase with grain size refinement is accompanied by a reduction in ductility, the underlying failure mechanism may change to fracture, e.g. resulting in progressive crushing [20], catastrophic failure [20] or localized end fracture [7,8] of the hollow cylinders. However, the nature of the interaction between the two failure mechanisms is unclear, and so is their effect on the macroscopic strength of the cylinder. This is partially due to the unclear scaling of ductility with grain size. While the failure strain of nanocrystalline materials is typically lower than that of their polycrystalline counterparts [21–26], there exists a plateau in the nanocrystalline regime (10-80 nm) [25,26] where the intrinsic ductility ceases to be sensitive to grain size and becomes instead a strain-controlled phenomenon.

The mechanisms that control the compressive deformation of thin-walled nanocrystalline tubes are therefore influenced by properties in the microstructural and macroscopic length scales. This study provides a first examination of the effect of grain size on the inherent failure mechanisms and strength of these cylinders. Uniaxial compressive tests of specimens with two typical grain sizes (20 nm and 100 nm) are used to report the achieved strength and discuss its dependence on geometric and material properties. Finite element calculations are also conducted to gain insights into the interaction between macroscopic (structural) and microscopic (material) failure, with fracture described through a void growth model.

2. Methods

2.1. Experimental

Polymer substrate cylinders with radius of 3.5 mm were metallized and electroplated to varying thicknesses using a pulsed-current electrodeposition process; details of the procedure can be found in Refs. [27,28]. After electrodeposition the substrates were mechanically removed, resulting in standalone Ni hollow cylinders of inner radius 3.5 mm and four sets of wall thicknesses in the range of 42 ± 1 μm to 382 ± 3 μm, shown in Table 1 (for simplicity, the thicknesses are hereafter referred to as 40, 80, 190 and 380 μm). Two sample sets were fabricated, one having an average grain size of 19 ± 7 nm (hereafter referred to as 20 nm Ni) and the other having a grain size of 108 ± 35 nm (henceforth referred to as 100 nm Ni); these grain sizes are typical of Ni electroplated with these conditions [29,30]. The Ni tubes were then sectioned into specimens of 20 mm length and subsequently tested in uniaxial compression at a constant strain rate of 10^{-3} s^{-1}. To get statistically significant observations, at least five specimens for each grain size/thickness combination were tested.

For mechanical and microstructural characterization, flat sheets of free-standing Ni were also deposited using the same conditions. The microstructure was characterized by transmission electron microscopy (TEM) with electron transparent foils produced by twin-jet electropolishing. Bright-field TEM images of the two microstructures are presented in Fig. 1. The tensile properties of the two materials were obtained by testing coupons of a standard geometry at a strain rate of 5×10^{-4} s^{-1} (see Ref. [26] for details); the reference tensile curves are shown in Fig. 2. The 20 nm grain size material had a 0.2% offset yield strength of 872 MPa and an elongation to failure of 0.06, whereas the 100 nm grain size material possessed a yield strength of 490 MPa and an elongation to failure of 0.16 [26].

Table 1. Summary of grain size, cylinder thickness (t), peak nominal strength (σ_N^{PK}), and failure mechanisms observed in the experimental tests and FE calculations of this study.

		Experimental		FE calculations	
Grain Size	t (μm)	σ_N^{PK} (MPa)	Failure mechanisms	σ_N^{PK} (MPa)	Failure mechanisms
20 nm	42 ± 1	524 ± 216	4 fold	957	4 fold
	81 ± 1	847 ± 147	4 fold	1137	4 fold/failure
	191 ± 7	1323 ± 177	fracture	1377	2 fold/axi./failure
	382 ± 3	1294 ± 93	fracture	1445	axi./failure
100 nm	44 ± 2	346 ± 99	4 fold	507	4 fold
	86 ± 1	502 ± 50	4 fold/3 fold	560	4 fold/3 fold
	176 ± 2	526 ± 26	3 fold/axi.	601	3 fold/axi.
	372 ± 3	654 ± 21	2 fold/axi.	686	2 fold/axi.

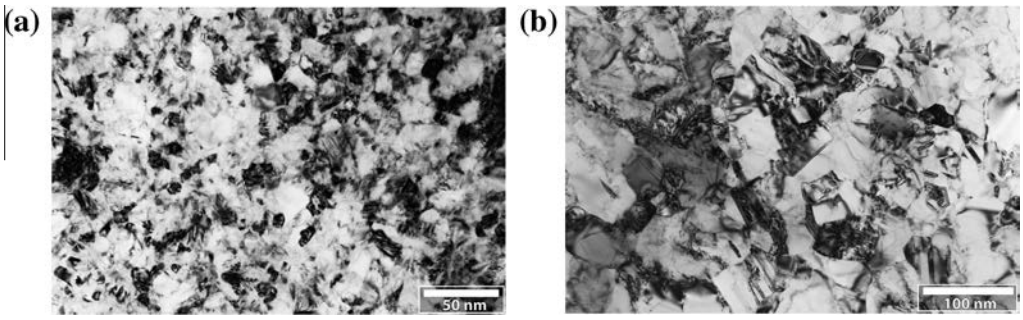

Fig. 1. Bright-field TEM micrographs of the microstructure of as-deposited Ni sheets with grain sizes 20 nm (a) and 100 nm (b).

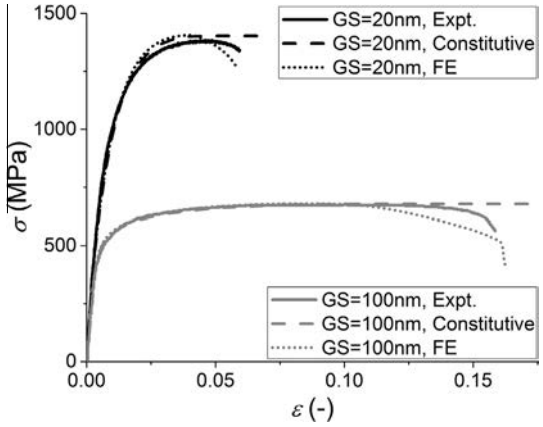

Fig. 2. Tensile engineering stress (σ)–strain (ε) curves of experimental tensile coupons with a grain size of 20 nm and 100 nm [26], constitutive material relationships of the FE model, and FE simulations of tensile tests with the failure model used in this study.

2.2. Finite element modeling

Uniaxial compression of the Ni cylinders was modeled using the finite element (FE) method; a typical geometry and mesh are shown in Fig. 3. Compression was simulated by positioning the tube between two analytical rigid surfaces; the bottom surface is constrained in all degrees of freedom, whereas the top surface is prescribed a displacement of -5.0 mm (nominal compressive strain of 0.25) in the global Y direction. A coefficient of friction $\mu = 0.6$, typical of steel (compression platens)/Ni (specimen) interfaces [31] was used to model the interaction between the rigid surfaces and the cylinder. Linear hexahedral elements with reduced integration and enhanced hourglass control were used in all models. The mesh contained at least five through-thickness elements and was biased in plane to produce a finer element size close to the upper and lower edges where local buckling typically initiates (average ratio of element to cylinder length $\sim 5.0 \times 10^{-3}$). Mesh convergence studies indicated that this level of refinement is adequate. Due to the large number of degrees of freedom, the problem was solved using the explicit solver of the commercial ABAQUS software with a time step of 0.005 s. The dynamic effects were minimal; the ratio of kinetic to internal energy was $<5 \times 10^{-4}$ in all models. Constitutive material properties for the FE calculations were specified by fitting the experimental tensile curves of Fig. 2 to analytical stress–strain relationships: the 20 nm grain size material was defined by a Voce hardening law, $\sigma = \sigma_\infty - (\sigma_\infty - \sigma_Y)\exp(-C\varepsilon)$, with $E = 167$ GPa, $\sigma_\infty = 1480$ MPa, $\sigma_Y = 104$ MPa, and $C = 90$ ($R^2 = 0.991$), whereas the 100 nm grain size material was defined by a Hollomon power law, $\sigma = K\varepsilon_P^n$, with $E = 124$ GPa,

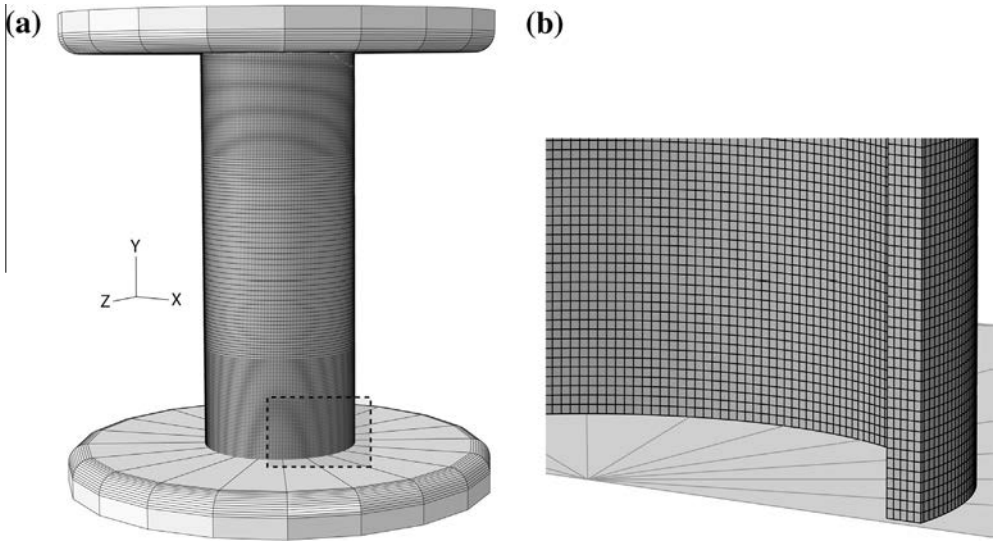

Fig. 3. FE assembly, showing rigid compressive surfaces and finite element mesh of the cylindrical model (a), and a close-up of the platen–cylinder interface (b).

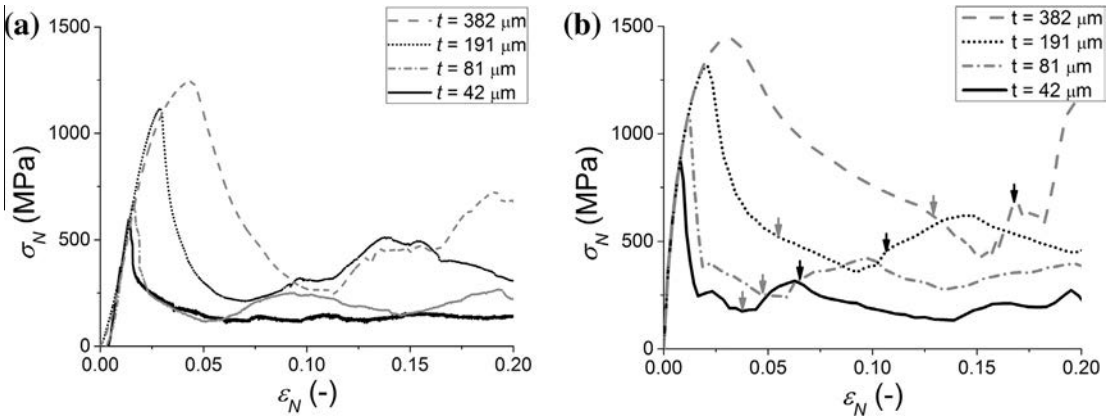

Fig. 4. Experimental (a) and FE simulated (b) nominal stress (σ_N)–strain (ε_N) curves of 20 nm grain size cylinders with wall thicknesses $42 \leqslant t \leqslant 382$ μm. The first activation of the critical (f_{CR}) and failure (f_F) void volume fractions is shown in (b) by the grey and black arrows, respectively.

$K = 951$ MPa and $n = 0.101$ ($R^2 = 0.992$); both relationships are shown in Fig. 2. Different hardening laws were chosen for the two grain sizes based on quality of their fit to the experimental data.

Material fracture was implemented within the FE calculations using the Gurson–Tvergaard–Needleman (GTN) model [32–35], which has been used in several studies of multiaxial stress states to model ductile fracture due to coalescence of microvoids (e.g. Refs. [36–38]). As described in the Appendix, the evolution of the yield surface is modified by the introduction of material parameters (q_1, q_2, q_3), the void volume fraction (f) and the effective porosity (f^*). The evolution of the void volume fraction is strain-controlled, and loss of stiffness in an element commences when the value of f becomes equal to a critical value f_{CR}; microscopically the achievement of this criterion corresponds to the initiation of void coalescence. Complete loss of stiffness and element removal is prescribed when the void volume fraction reaches the failure value f_F at all integration points; macroscopically this criterion corresponds to fracture propagation.

In summary, the GTN model uses eight material inputs to define: the yield surface (q_1, q_2, q_3), the void nucleation (ε_N, S_N, f_N) and failure (f_{CR}, f_F). The parameters that represent the behaviour of most metals are $q_1 = 1.5$, $q_2 = 1.0$, $q_3 = 2.25$, $\varepsilon_N = 0.3$, $S_N = 0.1$, $f_N = 0.04$, $f_{CR} = 0.15$, $f_F = 0.25$ [33]. It is worth noting that a large variation exists in the literature among the values of these parameters [39], and the most commonly modified are f_N, which defines the magnitude of the void nucleation rate, and f_{CR} and f_F, which define the critical and failure void volume fractions.

To calibrate these parameters, FE simulations of the tensile response of a standard coupon (geometry in Ref. [26]) were carried out to fit the post-necking portion of the curves; the results are shown in Fig. 2. It can be seen that overall trends are captured well by the model. The best-fit parameters were determined as $f_N = 0.14$, $f_{CR} = 0.15$, $f_F = 0.25$ for the material with a grain size of 20 nm, and $f_N = 0.02$, $f_{CR} = 0.15$, $f_F = 0.25$ for the material with a grain size of 100 nm (all other parameters were chosen as described in the original GTN work [33]).

3. Results and discussion

We first present the achieved compressive strength and analyse its dependency on material and geometrical properties for the case of macroscopic (i.e. buckling) failure. Subsequently, we describe the effect of material fracture, interaction between the failure mechanisms and implications for materials design.

3.1. Macroscopic failure

Fig. 4 presents the experimental and FE force–displacement relationships of specimens with the 20 nm grain size material, normalized by the cylinder's wall cross-sectional area and length, respectively (hereafter defined as nominal stress, σ_N, and nominal strain, ε_N, respectively). The achievement of material failure criteria (critical and failure void volume fractions) is marked by grey and black arrows, and is discussed in detail in Section 3.2. For the range of geometries investigated here, the experimental peak strengths of cylinders with 100 nm and 20 nm grain size were in the range of 350-650 MPa and 500-1300 MPa, respectively, while the corresponding FE values were in the range of 500-670 MPa and 950-1450 MPa, respectively, as summarized in Table 1.

The critical stress (σ_{CR}) of a cylindrical shell undergoing inelastic local buckling is given by [40,41]:

$$\sigma_{CR} = \frac{\alpha E t}{R}\left\{3\left[(5-4\nu)\frac{E}{E_T} - (1-2\nu)^2\right]\right\}^{-1/2} \quad (1)$$

where E, E_T and ν are the elastic modulus, tangent modulus (at the critical strain) and Poisson's ratio of the material, respectively, and t and R are the cylinder's thickness and radius. Upper and lower boundaries can be defined based on the end constraint of the shell; $\alpha = 2$ for simply supported ends (possessing only rotational degrees of freedom) and $\alpha = 1$ for free edges (having both rotational and translational degrees of freedom). Since the frictional coefficient between the platen and tube ends is finite ($\mu_{Ni/Steel} = 0.6$ [31]), it is expected that the experimental peak strengths will be between these upper and lower boundaries.

The peak strength of experiments, FE models and corresponding analytical predictions from Eq. (1) are summarized in Fig. 5a. There is good agreement between FE calculations and analytical predictions of Eq. (1). For instance the FE-predicted peak strengths at $t = 40$ μm are found to be within 99% of the values predicted by the simply supported edge assumption. This is because the frictional coefficient is sufficiently large to prevent lateral

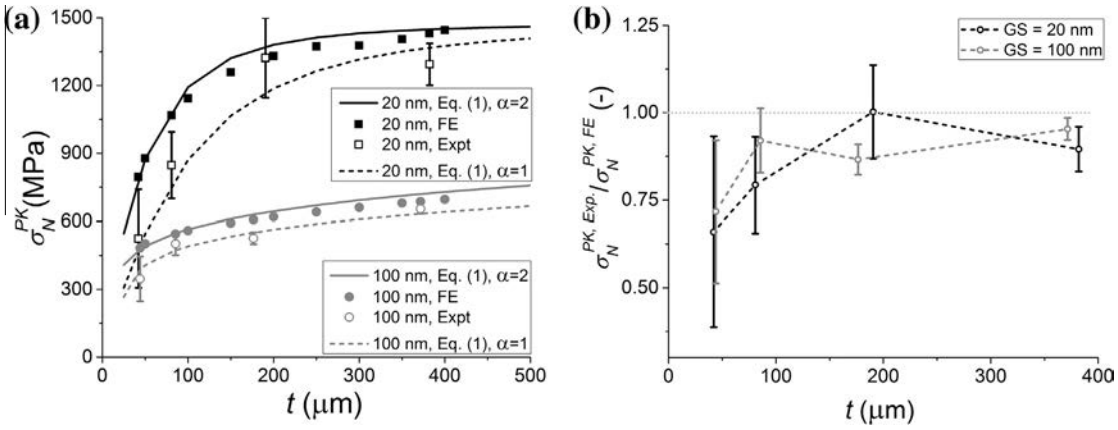

Fig. 5. Experimental, FE, and analytically predicted nominal peak strength (σ_N^{PK}) for free and simply supported edge conditions (a), and ratio of experimental to FE peak strength ($\sigma_N^{PK,Exp.}/\sigma_N^{PK,FE}$) (b) as a function of wall thickness (t).

translation of the edges before local buckling. As the thickness increases, some lateral translation becomes possible before buckling, and hence the peak strengths are bounded by the upper and lower limits of Eq. (1). Clearly, both the simply supported ends assumption of Eq. (1) and FE calculations overestimate the experimental peak strengths, particularly in the low thickness regime. This discrepancy has been reported elsewhere [42–44] and has been attributed to the sensitivity of shell buckling to imperfections, e.g. in this case, thickness non-uniformities, co-deposited particulate, and surface defects due to substrate non-uniformities (e.g. Ref. [45]). Cylinders with higher R/t ratios show a higher sensitivity to thickness non-uniformities [44], which can also be observed from the results of the present study, e.g. the ratio of experimental to FE peak strengths approaches unity with increasing wall thickness (Fig. 5b). This trend suggests that the defect sensitivity of the cylinders is determined by geometric properties rather than grain size.

Global buckling and local shell buckling are competing macroscopic failure mechanisms for columns under compressive axial loads. The global buckling critical strength is expressed by the Shanley–Engesser equation as [46]:

$$\sigma_{CR} = k^2\pi^2\frac{E_T I}{AL^2} \tag{2}$$

where I, A and L are the second moment of area, cross-sectional area and length of the cylinder, respectively, E_T is the tangent modulus of the material at the critical strain (in the elastic regime $E_T = E$) and k is a constant that describes the rotational constraint of the ends of the cylinder. Assuming rigid ends ($k = 2$), the critical stress of the hollow column can be expressed in terms of non-dimensional geometrical parameters as:

$$\sigma_{CR} = \pi^2\left(\frac{R}{L}\right)^2\left(\left(1+\frac{t}{R}\right)^2+1\right)E_T \tag{3}$$

When the critical stress for the two mechanisms is the same, failure could occur by either route and this can be used to define a boundary between the active zones on a failure mechanisms map (Fig. 6a). In the case of the geometries considered here ($L/R = 5.7$ and $0.01 \leqslant t/R \leqslant 0.1$) the critical stress for global buckling is 1.1 to 3.5 times higher than the critical stress for local shell buckling, thus the shell buckling mechanism will be activated first.

It is important to notice that for $t/R \geqslant 0.03$, the local buckling stress is in the inelastic regime of both materials. Within this regime, the strength increase due grain size reduction is a compound function of the material parameters that define the hardening law, the geometrical parameters (i.e. t/R and L/R) and governing failure mechanisms

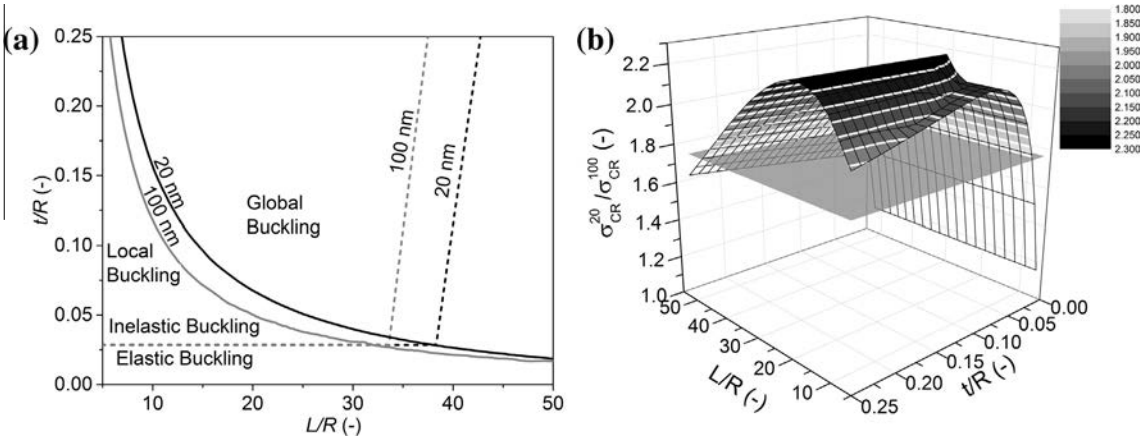

Fig. 6. Dependence of failure mechanisms (a) and ratio of critical strengths (b) on the thickness to radius (t/R) and length to radius (L/R) ratios of cylinders with a grain size of 20 nm and 100 nm.

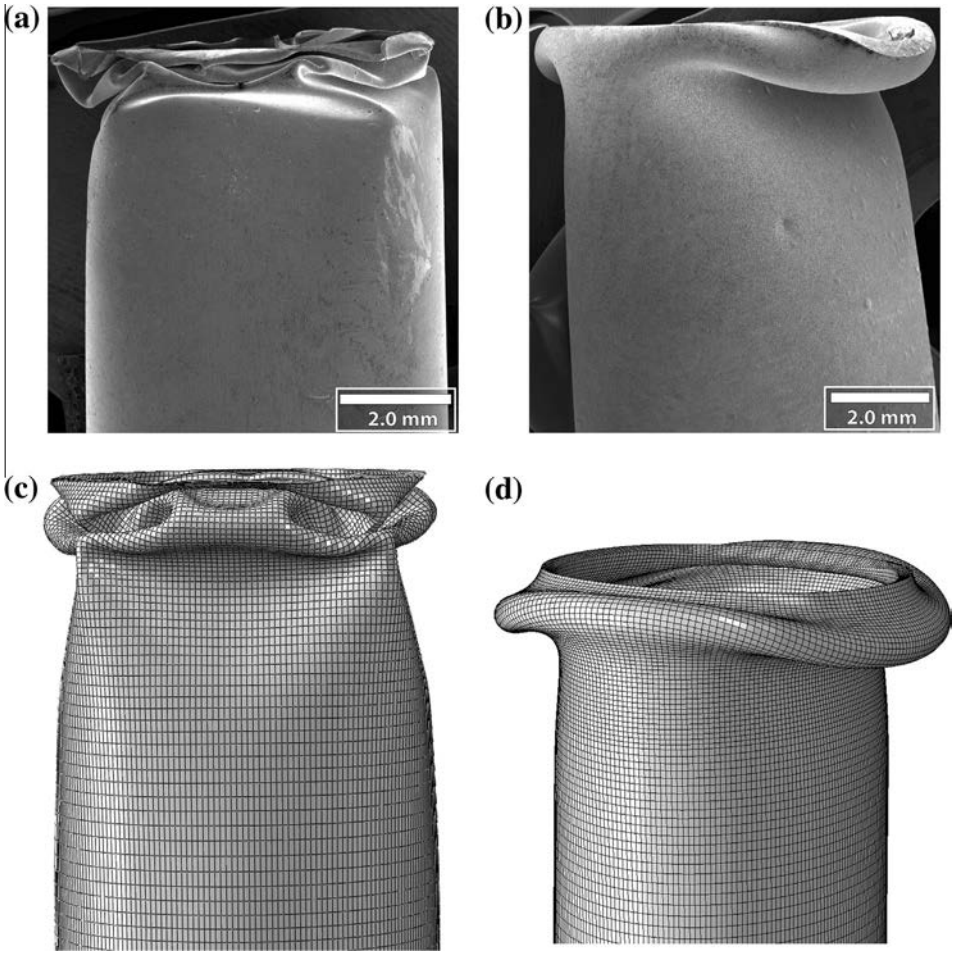

Fig. 7. Post-buckled deformation of specimens with grain size 100 nm and wall thickness 44 μm and 372 μm ((a) and (b), respectively), and deformation in FE models of the same wall thickness ((c) and (d), respectively).

(i.e. global or local buckling). Together, they determine the values of the critical strains at instability (which are distinct among cylinders of identical geometry but different material properties), and consequently the values of tangent moduli and critical strengths. In Fig. 6b, the critical strength ratio of the two materials is plotted over the geometry space defined by the two dimensionless parameters, along with the yield strength ratio as a reference. This ratio suggests that the increase in the column's critical stress due to grain size refinement can be even higher than the increase in the material's inherent yield strength.

In an idealized lattice unit cell composed of these cylinders, the out-of-plane compressive strength is proportional to the column's critical stress [47]. Experimental studies and finite element calculations [15,48] have furthermore indicated that both the mechanical strength and local buckling modes of unidirectional strut members are representative of the respective properties of inclined struts. Therefore the results of this study can be expected to be predictive of the properties of nanocrystalline hollow strut members in lattices of different orientations.

Fig. 6b also contains important information about the interaction of the strut's material and geometric properties, their effect on the macroscopic buckling mode and their consequence on the structural strength. At low L/R ratios, instabilities occur in both materials by local shell buckling. Within this regime, very thin ($t/R \leqslant 0.03$, or $t \leqslant 105$ μm for the current radius) cylinders will exhibit buckling in the elastic regime of the material, i.e. the instability sequence will be shell buckling followed by yielding (S–Y); examples of lattices with such geometries can be found in Refs. [7,8]. In this geometrical regime, the strengthening benefit provided by the material's grain size reduction is limited by the ratio of elastic moduli (1.34) and that of yield strengths (1.78) for the two grain sizes. However, when shell buckling occurs in the inelastic regime (i.e. with sequence Y–S), the strengthening effect of grain size reduction can be larger than the yield strength ratio, due to the value of the tangent moduli at the critical strain. For the materials and architectures considered here, the maximum strength ratio is achieved at a t/R of 0.09, and has a value of 2.2. As the slenderness ratio of the cylinder increases further, the instability mechanism transitions to global buckling (G), and when this instability occurs in the inelastic regime of the material (i.e. Y–G sequence), even higher strength ratios are possible (e.g. a maximum value of 2.3 is predicted at $L/R = 17.5$ and $t/R = 0.25$). These results show that in cases when the mechanical performance of the tubular network is governed by buckling instabilities, significant structural benefits can be achieved by reducing the grain size of structural members.

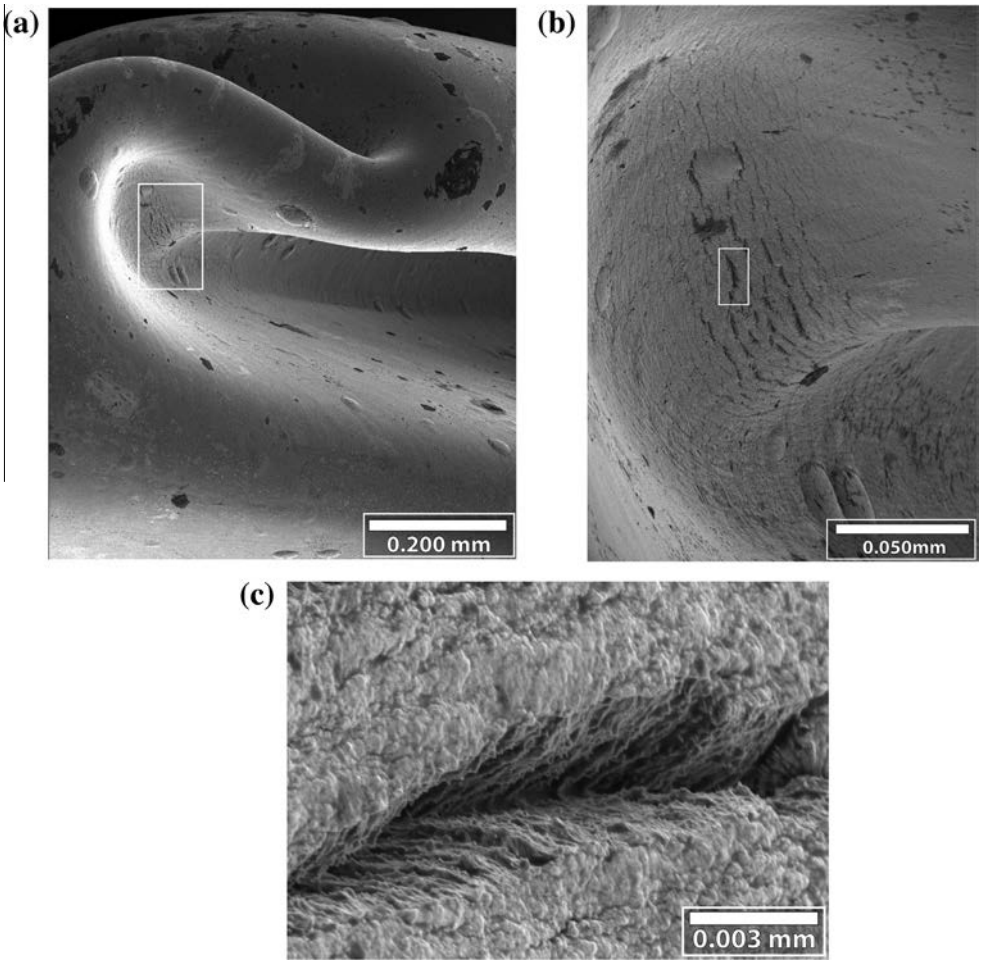

Fig. 8. Fracture surfaces in the four-fold buckled region of a specimen with grain size 20 nm and wall thickness 81 μm, at a nominal compressive strain of 0.20.

3.2. *Effects of material fracture*

The failure mechanisms that ultimately determine the mechanical properties of nanocrystalline cylindrical shells are: local buckling, activated at the mm length scale due to bifurcation in the stability path, and material fracture, activated at the nanometre scale (in nanocrystalline materials) due to transgranular microvoid coalescence, cleavage or intergranular fracture. These regimes are dependent on both geometrical and material properties. Andrews et al. [49], Guillow et al. [50] and Pingle et al. [48] have defined deformation mechanism maps for cylinders made of an annealed Ht-30 aluminium alloy, 6060-T5 aluminium alloy and 304 stainless steel, respectively. The cylinder's slenderness ratio (L/R) and the normalized wall thickness (t/R) dictate the following buckling mechanisms: global (elastic or plastic) buckling (predominant in struts with high L/R), barreling or buckling in a single axisymmetric mode (predominant in struts with low L/R) and gradual crushing through local shell buckling. The above failure mechanisms can occur in either the elastic or the inelastic regime of the material, bringing to six the total number of buckling modes. An important conclusion of these studies is that strain hardening can have a significant influence in both the deformation mechanism map and the achievable mechanical properties [48].

Among the samples tested in this study, all samples with grain size of 100 nm failed by local buckling in the concertina geometries, a phenomenon typically exhibited by cylindrical shells [51]. The number of lobes in each fold decreased from four to zero (denoting axisymmetric folding) as the wall thickness was increased from 40 μm to 380 μm; Table 1 summarizes the details of each buckling mode. Fig. 7a and b shows typical examples of four and two lobed folds in samples with wall thicknesses of 44 μm and 372 μm, respectively. In all cases, the deformation shape predicted by FE simulations matched that seen experimentally (e.g. see Fig. 7c and d), indicating the high fidelity of FE simulations in predicting macroscopic deformation.

Among cylinders with 20 nm grain size, all specimens exhibited material fracture over discrete regions of the post-buckled folds. In specimens with wall thicknesses of 40 μm and 80 μm, the fracture surfaces did not penetrate the thickness of the cylinder, even after the development of multiple longitudinal folds (e.g. four to five folds in compression to half of the initial height). Fig. 8 shows an example of this type of distributed fracture event in a specimen with wall thickness of 80 μm, deformed to a nominal compressive strain of 0.20. The fracture surfaces (Fig. 8b and c) are indicative of ductile fracture due to microvoid coalescence, and the parallel trails left behind in the opposing

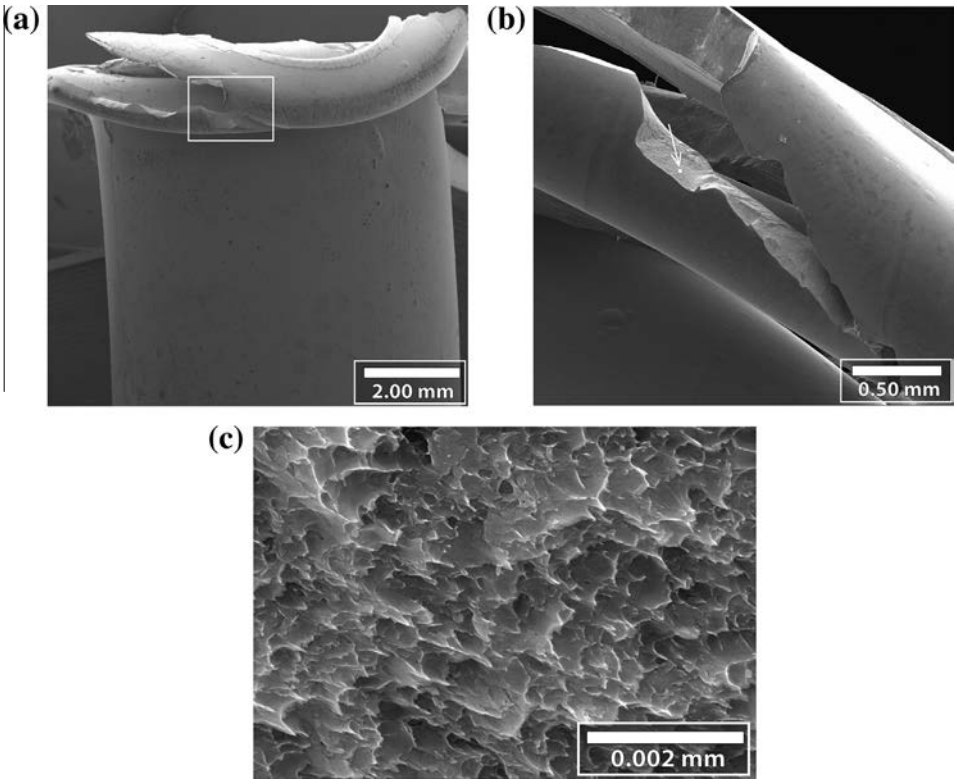

Fig. 9. Fracture surfaces in the axisymmetric buckled region of a specimen with grain size 20 nm and wall thickness 382 μm, at a nominal compressive strain of 0.20.

surfaces suggest that failure occurred due to tearing produced by a non-uniform stress state, starting at the free surface and propagating inwards.

In samples with larger wall thickness (i.e. 190 μm and 380 μm), fracture surfaces penetrated the thickness of the specimens and global deformation occurred by propagation of these macroscopic cracks instead of progressive local buckling. Fig. 9 shows one example of this type of fracture in a specimen with wall thickness of 380 μm. The fracture surface is a clear example of ductile failure due to microvoid coalescence; furthermore the equiaxed distribution of the void pits is indicative of fracture propagation due to a primarily tensile stress state. This type of stress state is expected to follow the later stages of the development of an axisymmetric fold due to the uniform distribution of bending stresses in the free surface at the apex of the concave fold.

The ductile nature of fracture validates the use of the microvoid-based failure model within the FE calculations. In these calculations, loss of stiffness commences when the void volume fraction in an element reaches the critical value (f_{CR}), and crack propagation is modeled through the removal of elements where the void volume fraction reaches the failure value (f_F) at all integration points. The maximum void volume fraction in models with the 100 nm grain size material was found to be below the $f_{CR} = 0.15$ threshold for all wall thicknesses, which is consistent with the experimental observations. By contrast, the critical void volume fraction was reached in at least one element in all models with grain size of 20 nm. The strains at which the critical and failure void volume fractions were reached in these simulations are shown in grey and black arrows in the stress–strain curves of Fig. 4b. Note that the activation of the fracture mechanism occurs during the end of the first peak of the stress–strain curve, which macroscopically corresponds to the formation of the first half of the full fold, i.e. when the strain state at the surface reaches the maximum tensile value in both the longitudinal and radial directions. At a nominal axial strain of 0.2 (the amount of experimental strain in Figs. 8 and 9), the critical void fraction was exceeded for all four 20 nm grain size wall thicknesses. Moreover, the failure void fraction was exceeded in all models with wall thickness larger than 81 μm, in agreement with experimental observations.

It is worthwhile to point out that since the mesh of these models is static, there is a limitation in the prediction of the evolution of crack propagation. The concave surface in a fold is always in a compressive state, thus the yield surface of these elements is modified such that they can display strain hardening due to the closure of existing voids. Therefore, the strain distribution in these elements does not allow the achievement of the critical void volume fraction, and the propagation of the fracture path through the thickness cannot be modeled accurately. Nonetheless, this limitation influences only the late stages of crack propagation, and these FE models can be considered sufficient to predict the initiation of macroscopic fracture. For instance, Fig. 10 shows the circumferential band of removed elements in a model with wall thickness of 382 μm; good agreement is observed in the planar path of the facture surface compared with the experimental observation (Fig. 9a).

A connection can be made between the symmetry of the buckling folds, the strain evolution, and the initiation of fracture. We first look at the way that grain size and cylinder geometry influence the symmetry of the local shell

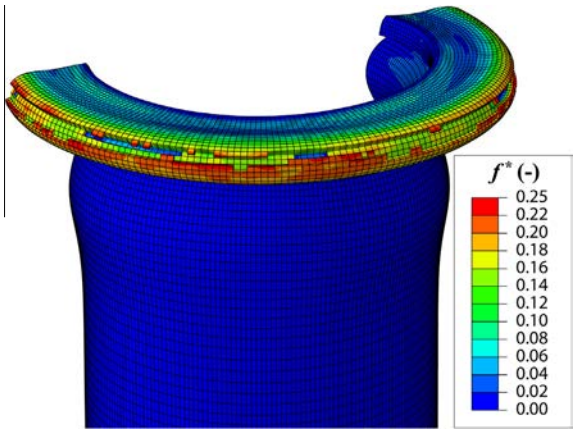

Fig. 10. Deformation mode and distribution of void volume fraction (f^*) in a FE model with grain size 20 nm and wall thickness 382 μm at a nominal compressive strain of 0.20, showing element removals due to the ductile failure model ($f^* > f_F = 0.25$).

buckling mechanism. Previous experimental results [47–54] have shown that in thin-walled tubes (e.g. $0.02 < t/R < 0.2$), the number of lobes within a fold increases with decreasing wall thickness, e.g. from zero (purely axisymmetric concertina) to four (purely diamond folds). In the range of current geometries this was also observed – the thinnest cylinders ($t/R \approx 0.01$) displayed purely four-fold symmetry, and the thickest ones ($t/R \approx 0.1$) failed in an axisymmetric concertina symmetry; mixed modes were also observed, both within groups of specimens with the same approximate thickness and within individual specimens (see Table 1). Collapse in the diamond mode in the thinnest cylinders ($t/R \approx 0.01$; $L/R \approx 5.7$) and two-fold/axisymmetric buckling modes in the thickest cylinders ($t/R \approx 0.1$; $L/R \approx 5.7$) are in good agreement with the deformation mechanism maps of Refs. [48–50], as is the transition into axisymmetric crushing with increasing t/R. Notice, however, that in spite of the large difference in yield strength and hardening coefficient in the two materials considered here, the geometry of the buckling folds is similar within specimen groups of the same thickness. This suggests that the resultant buckling shape is more sensitive to the geometry of the cylindrical shell than the grain size of the material.

We next consider the effect of buckling mode on the strain distribution developed during gradual collapse. The evolution of the maximum value of longitudinal and circumferential strains with nominal compressive strain is shown in Fig. 11a and b respectively, for FE models with thickness 50 μm and 300 μm and grain sizes 20 nm and 100 nm. In these models, those with 50 μm wall thicknesses buckled in a four-fold symmetry, whereas those with 300 μm thickness buckled in two-fold symmetry for a grain size of 20 nm and axisymmetric for a grain size of 300 nm. The maximum circumferential strain decreases with increasing thickness, due to the smaller number of lobes and the reduction in stress concentration sites. The opposite trend is observed in the longitudinal strains, because the rate of change of curvature in the longitudinal direction of the entire fold is larger in the absence of kinks (e.g. see Fig. 7). Notice that the maximum strains are similar across models with the same thickness; this is to be expected, because the strains developed in the model depend on the buckling geometry.

The initiation of failure will therefore be determined by the evolution of the void volume fraction with the geometry-dependent strain state mentioned above. Fig. 12a and b shows the evolution of the maximum value of the void volume fraction, and nominal stress–strain curves, in models of thickness 50 μm and 300 μm respectively, and the maximum achieved void volume fraction and buckling geometries for all simulations of this study are summarized in Fig. 12c. In spite of similar buckling modes and strain distributions among samples of similar thickness, the evolution of the ductile damage criterion is significantly different. The strains reached in these models are insufficient to cause appreciable void growth in any of the models with grain size of 100 nm. However, even the thinnest of specimens with a grain size of 20 nm can achieve the critical void volume fraction required for failure initiation ($f_{CR} = 0.15$).

An important design issue for hollow structural members of grain-refined materials is the interaction between the failure mechanisms (shell buckling and fracture) and the effect of each on structural performance criteria (e.g. weight-specific strength, stiffness, energy absorption etc.). During axial deformation, shell buckling precedes fracture; e.g. the strains at which fracture initiation occurs (Fig. 4b) are in all cases larger than the peak strain. This sequence of failure mechanisms can be expected in all loading

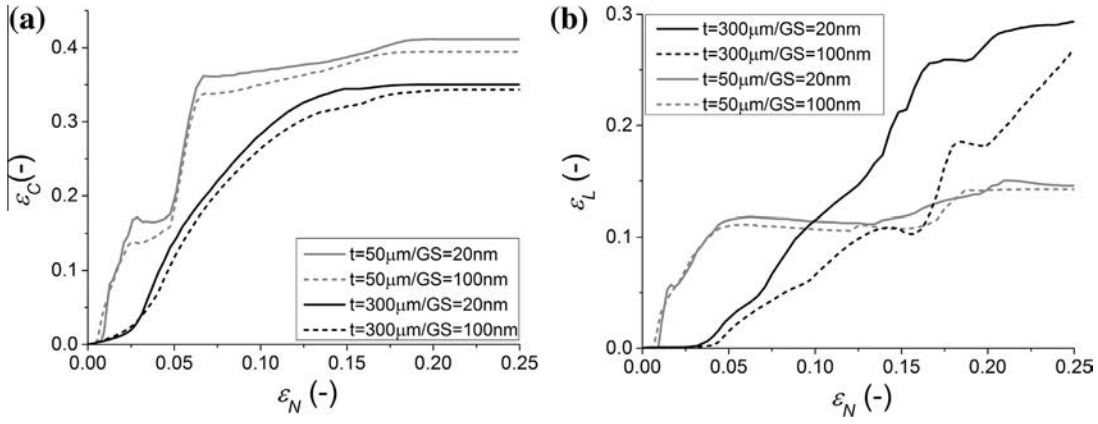

Fig. 11. Evolution of maximum circumferential strain ε_C (a) and longitudinal strain ε_L (b) in FE models of thickness 20 μm and 300 μm and grain sizes 20 nm and 100 nm.

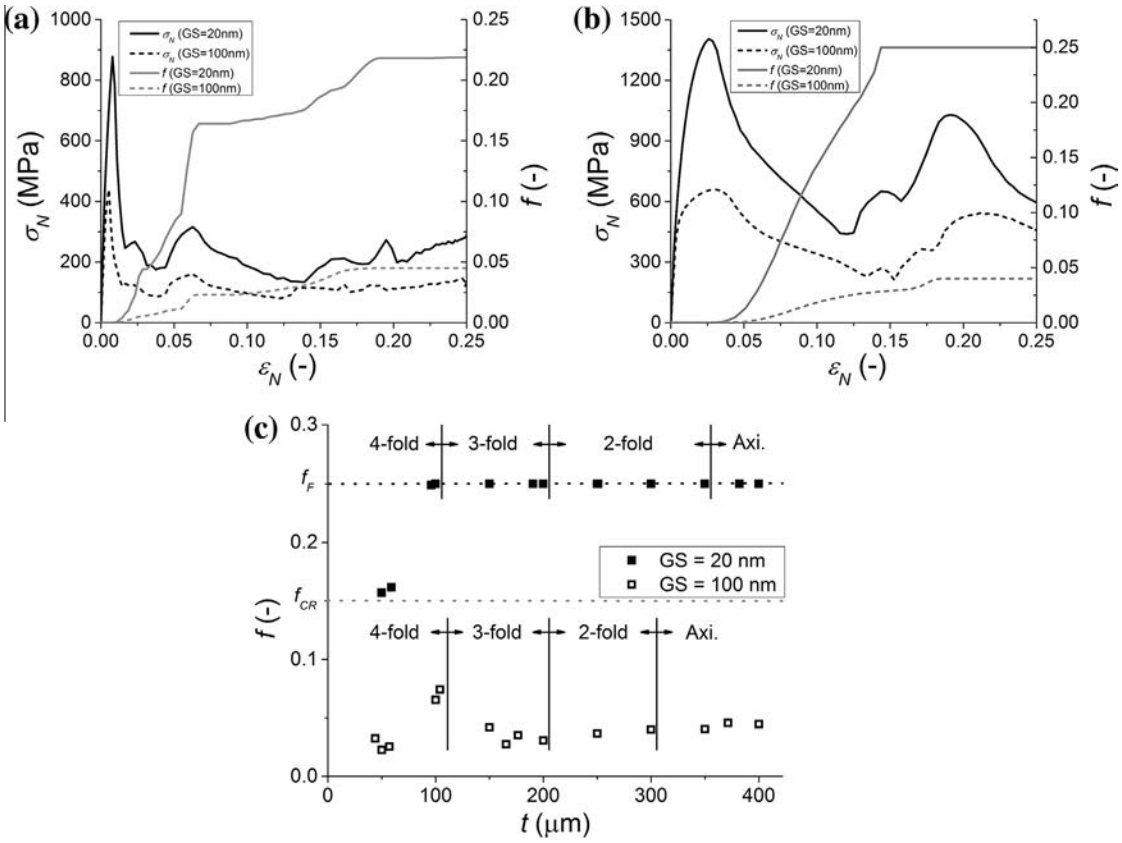

Fig. 12. Evolution of nominal stress (σ_N) and void volume fraction (f) with nominal strain (ε_N) in models of thickness 50 μm (a) and 300 μm (b), and summary of deformation modes and maximum achieved void volume fraction in all FE models of this study (c).

conditions where deformation is primarily compressive, because ductile failure due to the coalescence and growth of microvoids occurs in a tensile stress state, which in turn can only be introduced after the first local buckling fold has occurred. Since shell buckling is the determining factor in the load-bearing capacity of the structural member, the increase in the constituent material's flow stress can be beneficial. Therefore, in cases when the cylindrical component is designed not to deform past the peak compressive load (e.g. in truss assemblies that are used to support static loads), grain refinement can be an effective method to increase strength at no weight penalty.

The main drawback of grain size reduction is the limited ductility. Post-buckling fracture phenomena appear at later stages of the deformation, but are nevertheless significant in structural design. In many cases, cylindrical components are designed to support large scale deformation, e.g. energy absorption applications which exploit the periodic nature of gradual crumpling. In these applications, the large-strain behaviour (e.g. plateau stress) is far more significant than the behaviour during initial deformation, and the propagation of fracture surfaces can be detrimental for practical use. These issues are common to structural members made of similar ductility-limited materials, e.g. surface carburization has been used to harden appreciably the cylindrical struts of lattices, however at the expense of embrittlement [17]. Nevertheless, our study confirms that grain size refinement provides an additional useful variable in mechanical design space for these materials, i.e. the possibility to tailor the strength and ductility of the constituent material as dictated by design.

4. Conclusions

Hollow cylindrical struts created by nanocrystalline electrodeposition can support high compressive strengths due to the increased yield strength that results from the grain size reduction. In this study, cylinders of nanocrystalline Ni with grain sizes 20 nm and 100 nm showed two types of failure mechanisms: local buckling (with phenomena in the millimetre to centimetre scale) and material fracture (with phenomena in the nanometre to micrometre scale). Specimens fabricated with electrodeposited Ni of 20 nm grain size showed significantly higher (e.g. by a factor of 1.5-2.5) peak strengths compared to their 100 nm grain size counterparts of the same dimensions; however, their compressive behaviour was also accompanied by material fracture.

Finite element calculations were used to show that shell buckling and material fracture are not competing failure mechanisms; the initial instability is due to a shell buckling mechanism which is followed in the later stages of compression by material fracture. This sequence has two important implications. First, since the initial compressive strength of hollow cylinders is determined by shell buckling, the maximum supported static stress is dictated by the flow stress rather than ductility limitation of the inherent material. Subsequently, the benefits of grain size reduction can be exploited over the entire Hall–Petch regime. Second, when the buckling instability occurs in the inelastic range of the constituent material, the strength increase of the structural member can be even higher than the yield strength increase, due to the work hardening capacity of the nanocrystalline

material; in the two grain sizes considered in this study (ratio of yield strengths ≈1.8), a macroscopic strength increase by a factor of as much as 2.3 is possible for hollow structural members.

In the latter stages of compression, the gradual shell buckling is accompanied by the development of significant strain gradients; thus the material's ductility can influence the progression of deformation. In the specimens of this study, ductile fracture appeared as microcracks accompanying local buckling in relatively thin specimens (40 μm and 80 μm wall thickness), and as the primary deformation mode in thicker specimens (200 μm and 400 μm wall thickness). The geometry of the local shell buckling is sensitive to specimen geometry rather than grain size, e.g. the number of in-plane folds decreases with t/R ratios in both grain sizes. The magnitude of the strain gradient is also higher in cylinders with higher t/R ratios; thus in grain refined materials with limited ductility, the deformation of thick specimens proceeds through fracture propagation rather than progressive shell buckling.

From a materials design perspective, there exists a trade-off between the strength/weight benefits that are achieved with grain size reduction and the ductility limitations that will influence the later stages of deformation. For instance, in structural members that are designed to support static loads without buckling, grain size refinement can be useful in increasing the safe load at no weight penalty. Conversely, in applications where post-buckling deformation is the principal function of the design (as in energy absorbers), it is necessary to not go too far in the direction of grain size reduction; in these cases, energy dissipation through fracture propagation can be a drawback that outweighs the benefits of higher structural strength.

Acknowledgements

The authors are grateful to Mr Sal Boccia, Mr Dan Kraehling and Integran Technologies Inc. for the technical help with the synthesis, characterization and testing of nanocrystalline cylinders. Financial support was provided by the Natural Sciences and Engineering Research Council of Canada (NSERC); one of the authors (E.B.) was partially funded from the Dimitris N. Chorafas Foundation prize.

Appendix .

In the Gurson–Tvergaard–Needleman model for ductile fracture of porous metals, the yield function of the material is given by:

$$\mathbf{\Phi}(\boldsymbol{\sigma}, \bar{\varepsilon}^P, f) = \left(\frac{\bar{\sigma}}{\sigma_0(\bar{\varepsilon}^P)}\right)^2 + 2f^*(f)q_1 \cosh\left(\frac{-3q_2\sigma_H}{2\sigma_0(\bar{\varepsilon}^P)}\right) - (1 + q_3 f^*(f)) = 0 \tag{A.1}$$

where $\bar{\sigma}$ is the macroscopic von Mises stress, σ_0 is the equivalent stress in the undamaged material as a function of the equivalent plastic strain $\bar{\varepsilon}^P$, σ_H is the hydrostatic stress, q_1, q_2 and q_3 are material parameters that are introduced to improve the agreement with numerical studies of materials containing periodically distributed circular cylindrical or spherical voids [33–35] and f^* represents the effective porosity. The latter is a function of void volume fraction f, and has the form:

$$f^* = \begin{cases} f, & \text{for } f \leqslant f_C \\ f_C + \frac{f_F^* - f_C}{f_F - f_C}(f - f_C), & \text{for } f_C \leqslant f \leqslant f_F \\ f_F^*, & \text{for } f > f_F \end{cases} \tag{A.2}$$

where f_C is the critical void volume fraction at which coalescence starts, f_F is the final void volume fraction at fracture and $f_F^* = \frac{q_1 + \sqrt{q_1^2 - q_3}}{q_3}$. The rate of change of the void volume fraction is the sum of the nucleation ($\dot{f}_n$) and growth ($\dot{f}_g$) rates, which are given by:

$$\dot{f}_n = \frac{f_N}{S_N\sqrt{2\pi}} \exp\left[-\frac{1}{2}\frac{\bar{\varepsilon}^P - \varepsilon_N}{S_N}\right]\dot{\bar{\varepsilon}}^P \tag{A.3}$$

and

$$\dot{f}_g = (1 - f)\dot{\varepsilon}^P : \mathbf{I} \tag{A.4}$$

In Eqs. (A.3) and (A.4), f_N is the volume fraction of all particles with potential for microvoid nucleation, ε_N and S_N describe the distribution of void nucleation rate with equivalent plastic strain (mean strain and standard deviation respectively) and $\dot{\varepsilon}^P$ is the rate of change of the plastic strain.

References

[1] M.F. Ashby, Philos. Mag. 85 (2005) 3235.
[2] N.A. Fleck, V.S. Deshpande, M.F. Ashby, Proc. R. Soc. A 466 (2010) 2495.
[3] S.T. Brittain, Y. Sugimura, O.J.A. Schueller, A.G. Evans, G.M. Whitesides, J. Microelectromech. Syst. 10 (2001) 113.
[4] D.J. Sypeck, H.N.G. Wadley, Adv. Eng. Mater. 4 (2002) 759.
[5] Y. Boonyongmaneerat, C.A. Schuh, D.C. Dunand, Scripta Mater. 59 (2008) 336.
[6] M. Suralvo, B. Bouwhuis, J.L. McCrea, G. Palumbo, G.D. Hibbard, Scripta Mater. 58 (2008) 247.
[7] T.A. Schaedler, A.J. Jacobsen, A. Torrents, A.E. Sorensen, J. Lian, J.R. Greer, L. Valdevit, W.B. Carter, Science 334 (2011) 962.
[8] A. Torrents, T.A. Schaedler, A.J. Jacobsen, W.B. Carter, L. Valdevit, Acta Mater. 60 (2012) 3511.
[9] K. Maloney, C.S. Roper, A.J. Jacobsen, W.B. Carter, L. Valdevit, T.A. Schaeddler, APL Mater. 1 (2013) 022106.
[10] X. Zheng, H. Lee, T.H. Weisgraber, M. Shusteff, J. DeOtte, E.B. Duoss, J.D. Kuntz, M.M. Biener, Q. Ge, J.A. Jackson, S.O. Kucheyev, N.X. Fang, C.M. Spadaccini, Science 344 (2014) 1373.
[11] V.S. Deshpande, M.F. Ashby, N.A. Fleck, Acta Mater. 49 (2001) 1035.
[12] V.S. Deshpande, M.F. Ashby, N.A. Fleck, J. Mech. Phys. Solids 49 (2001) 1747.
[13] D.T. Queheillalt, H.N.G. Wadley, Acta Mater. 53 (2005) 303.
[14] D.T. Queheillalt, H.N.G. Wadley, Mater. Sci. Eng. A 397 (2005) 132.
[15] A.G. Evans, M.Y. He, V.S. Deshpande, J.W. Hutchinson, A.J. Jacobsen, W.B. Carter, Int. J. Impact Eng. 37 (2010) 947.
[16] D.T. Queheillalt, H.N.G. Wadley, Int. J. Mater. Res. 102 (2011) 389.
[17] L. St-Pierre, N.A. Fleck, V.S.D. Deshpande, Int. J. Solids Struct. 51 (2014) 41.
[18] B.A. Bouwhuis, J.L. McCrea, G. Palumbo, G.D. Hibbard, Acta Mater. 57 (2009) 4046.
[19] E. Bele, B.A. Bouwhuis, G.D. Hibbard, Acta Mater. 57 (2009) 5927.
[20] J. Lian, D. Jang, L. Valdevit, T.A. Schaedler, A.J. Jacobsen, W.B. Carter, J.R. Greer, Nano Lett. 11 (2011) 4118.
[21] N. Wang, Z. Wang, K.T. Aust, U. Erb, Mater. Sci. Eng. A 237 (1997) 150.

[22] H. Iwasaki, K. Higashi, T.G. Nieh, Scripta Mater. 50 (2004) 395.
[23] P.G. Sanders, C.J. Youngdahl, J.R. Weertman, Mater. Sci. Eng. A 234–236 (1997) 77.
[24] Y.M. Wang, E. Ma, M.W. Chen, Appl. Phys. Lett. 80 (2002) 2395.
[25] T.J. Massart, T. Pardoen, Acta Mater. 58 (2010) 5768.
[26] I. Brooks, G. Palumbo, G.D. Hibbard, Z. Wang, U. Erb, J. Mater. Sci. 46 (2011) 7713.
[27] U. Erb, A.M. El-Sherik, Nanocrystalline Metals and Processes of Producing the Same. US Patent 5,353,266, October 1994.
[28] U. Erb, A.M. El-Sherik, C.K.S. Cheung, M.J. Aus, Nanocrystalline Metals. US Patent 5,433,797, July 1995.
[29] A.M. El-Sherik, U. Erb, G. Palumbo, K.T. Aust, Scripta Mater. 27 (1992) 1185.
[30] A.M. El-Sherik, U. Erb, J. Mater. Sci. 30 (1995) 5743.
[31] J.R. Davis, Concise Metals Engineering Data Book, ASM International, Materials Park, OH, 1977.
[32] A. Gurson, J. Eng. Mater. Technol. 99 (1977) 2.
[33] V. Tvergaard, A. Needleman, Acta Metall. 32 (1984) 157.
[34] V. Tvergaard, Int. J. Fract. 17 (1981) 389.
[35] V. Tvergaard, Int. J. Fract. 18 (1982) 237.
[36] H. Li, M.W. Fu, J. Lu, H. Yang, Int. J. Plasticity 27 (2011) 147.
[37] S. Kimura, T. Mochida, T. Kawasaki, H. Nakamura, T. Yamaguchi, ASME 2011 International Mechanical Engineering Congress and Exposition, ASME, New York, 2012.
[38] L. Malcher, F.M.A. Pires, J.M.A.C. de Sa, Int. J. Plasticity 54 (2013) 193.
[39] N. Benseddiq, A. Imad, Press. Vessels Piping 85 (2008) 219.
[40] S.C. Batterman, Int. J. Solids Struct. 3 (1967) 501.
[41] S.C. Batterman, J. Appl. Mech. 35 (1968) 73.
[42] V. Tvergaard, Thin Wall Struct. 1 (1983) 139.
[43] F.M. Mazzolani, Aluminium Alloy Structures, second ed., Chapman and Hall, London, 1995.
[44] NASA SP-8007. Buckling of Thin-Walled Circular Cylinders. Washington, DC: National Aeronautics and Space Administration; 1968.
[45] M.J. Willey, U. Emekli, A.C. West, J. Electrochem. Soc. 155 (2008) D302.
[46] F.R. Shanley, J. Aero. Sci. 15 (1947) 261.
[47] V.S. Deshpande, N.A. Fleck, M.F. Ashby, J. Mech. Phys. Solids 49 (2001) 1747.
[48] S.M. Pingle, N.A. Fleck, V.S. Deshpande, H.N.G. Wadley, Proc. R. Soc. A 467 (2011) 985.
[49] K.R.F. Andrews, G.L. England, E. Ghani, Int. J. Mech. Sci. 25 (1983) 687.
[50] S.L. Guillow, G. Lu, R.H. Grzebieta, Int. J. Mech. Sci. 43 (2001) 2103.
[51] J.M. Alexander, Q. J. Mech. Appl. Math. 13 (1960) 10.
[52] A.G. Pugsley, M.A. Macaulay, Q. J. Mech. Appl. Math. 13 (1960) 1.
[53] J.T. Allan, J. Mech. Eng. Sci. 10 (1968) 182.
[54] W. Johnson, S. Reid, Appl. Mech. Rev. 31 (1978) 277.